

An Ultrafast and Stable High-Entropy Metallic Glass Electrode for Alkaline Hydrogen Evolution Reaction

Zhe Jia,* Yiyuan Yang, Qing Wang, Charlie Kong, Yin Yao, Qianqian Wang, Ligang Sun,* Baolong Shen,* and Jamie J. Kruzic*

Cite This: *ACS Materials Lett.* 2022, 4, 1389–1396

Read Online

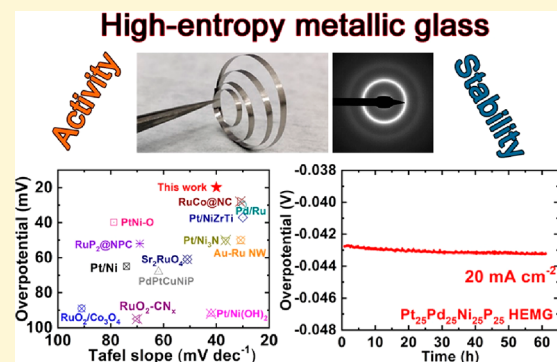
ACCESS |

Metrics & More

Article Recommendations

Supporting Information

ABSTRACT: A new type of high-entropy alloy with a composition of $\text{Pt}_{25}\text{Pd}_{25}\text{Ni}_{25}\text{P}_{25}$ (at.%) and an amorphous structure, referred to as a high-entropy metallic glass (HEMG), was developed by a scalable metallurgical technique for efficient hydrogen evolution reaction (HER). The achieved overpotential was as low as 19.8 mV at a current density of 10 mA cm^{-2} while maintaining an ultrareliable performance for 60 h in 1.0 M KOH solution, exhibiting 5- and 10-times higher performance than those of traditional $\text{Pt}_{60}\text{Ni}_{15}\text{P}_{25}$ and $\text{Pd}_{40}\text{Ni}_{40}\text{P}_{20}$ metallic glasses, respectively, and also surpassing the benchmark performance of commercial Pt/C nanoparticles and pure Pt sheet. Experimental and theoretical results revealed that the enhanced HER activity was ascribed to a synergistic function of multiprincipal components that optimized the electronic structure to accelerate the rate-determining steps in HER. Moreover, the unique long-range disordered structure provided a high density of unsaturated atomic coordination that was able to improve the amount of electrochemically active sites. This bulk HEMG strategy paves the way for the development of flexible freestanding electrodes for water splitting applications.



Water electrolysis is considered as one of the most promising alternatives to steam reforming for hydrogen production, because of its simplicity, zero carbon emissions, and attractive feedstock circulation.^{1–5} However, the state-of-the-art high-performance electrode materials recently developed for water splitting are based on carbon carriers mediated by binding active elements, e.g., Pt/C nanoparticles, and their complicated processing methods are a major impediment to the commercialization of this technology. Accordingly, it is currently a great challenge to design an effective electrocatalyst to overcome these significant problems.

High-entropy alloys (HEAs) containing four or more principal components alloyed into a stable crystalline solid-solution phase have demonstrated great potential for the discovery and development of alloys with novel properties for various applied fields.^{6,7} The properties of HEAs in harsh environments has been a subject of significant investigation, including elevated and cryogenic temperatures,⁸ corrosive environments,⁹ electrocatalytic environments,¹⁰ etc. Inspired by such successes, several HEAs have been reported as potential electrocatalysts exhibiting outstanding performance, including solid-solution HEAs¹¹ or high-entropy intermetallics

(HEIs)¹² for the hydrogen evolution reaction (HER) and oxygen microalloyed HEAs (O-HEAs) for the oxygen evolution reaction (OER).¹³ However, exploiting opportunities to further optimize the catalytic properties of HEAs by controlling the functional atoms within an amorphous structure is still a great challenge.¹⁴ The development of high-entropy metallic glasses (HEMGs) presents several opportunities in this regard, and it was found that HEMGs can demonstrate superiorities because of their long-range disordered structure^{15–18} and a high density of unsaturated atomic coordination.^{19–22} While HEMGs provide much promise to optimize the atomic configurations and enhance catalytic performance, achieving the goal of how to control the functional atoms and tune their synergistic effects to achieve

Received: April 26, 2022

Accepted: June 20, 2022

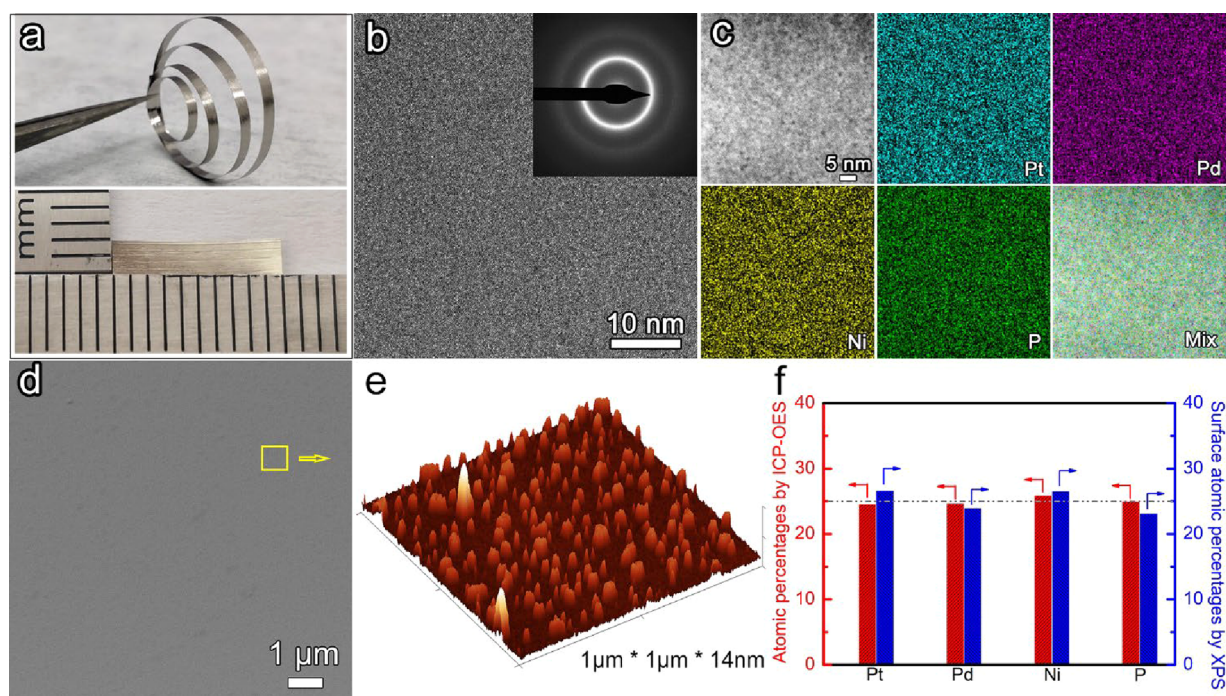


Figure 1. (a) Photographs, (b) HRTEM image (inset shows the SAED pattern), (c) HADDF-STEM mapping results, (d) SEM image, (e) AFM image, and (f) atomic compositions of the $\text{Pt}_{25}\text{Pd}_{25}\text{Ni}_{25}\text{P}_{25}$ HEMG.

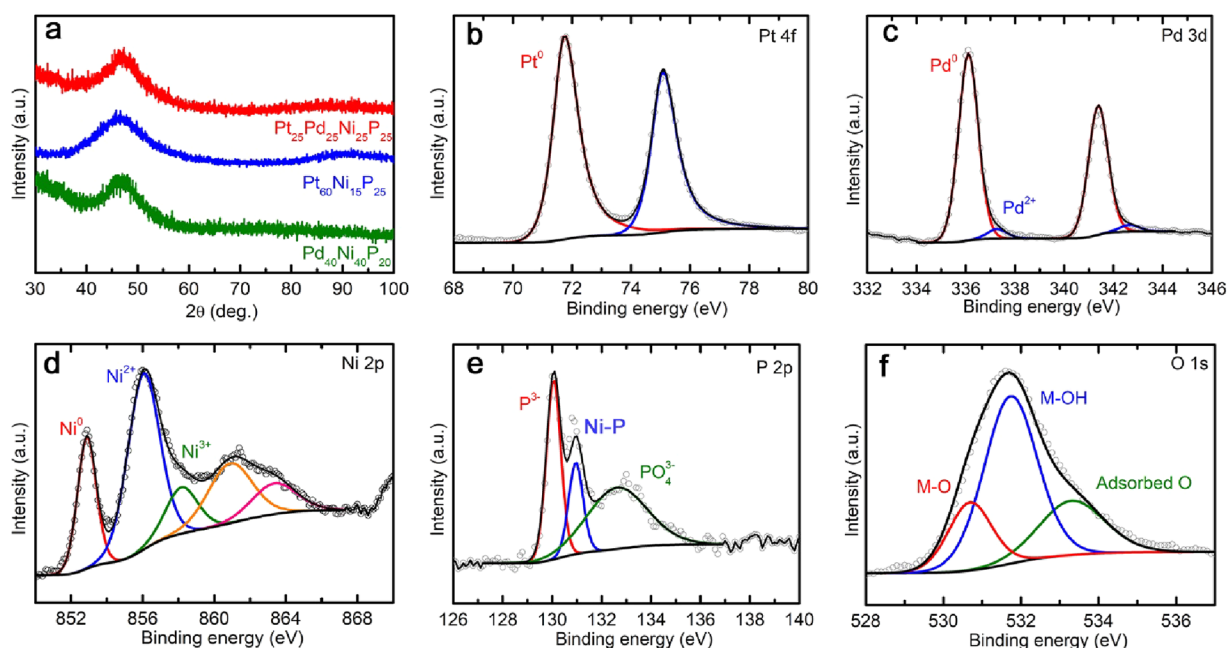


Figure 2. (a) XRD patterns of the three as-spun MGs, and high-resolution XPS spectra of (b) Pt 4f, (c) Pd 3d, (d) Ni 2p, (e) P 2p, and (f) O 1s for the $\text{Pt}_{25}\text{Pd}_{25}\text{Ni}_{25}\text{P}_{25}$ HEMG.

excellent functional properties is still an ongoing research challenge.

In this work, we employed a scalable melt-spinning technique to manufacture a flexible freestanding HEMG ribbon with an equiatomic composition of $\text{Pt}_{25}\text{Pd}_{25}\text{Ni}_{25}\text{P}_{25}$ that can be used directly as electrodes for HER. The primary objective was to investigate how the synergistic effect of having multiple, equiatomic functional atom types can promote the electrocatalytic performance. To achieve this goal, two traditional MGs with the atomic compositions of $\text{Pt}_{60}\text{Ni}_{15}\text{P}_{25}$

and $\text{Pd}_{40}\text{Ni}_{40}\text{P}_{20}$ were prepared for performance comparison. Figure 1b shows a high-resolution transmission electron microscopy (HRTEM) image and the corresponding selected area electron diffraction (SAED) pattern of the as-spun $\text{Pt}_{25}\text{Pd}_{25}\text{Ni}_{25}\text{P}_{25}$ HEMG shown in Figure 1a. The long-range disordered structure and amorphous diffraction halo are clearly observed. Figure 1c shows a scanning transmission electron microscopy (STEM) image with elemental mapping results. It was found that the Pt, Pd, Ni, P elements exhibited inhomogeneous contrast with dark and bright regions at

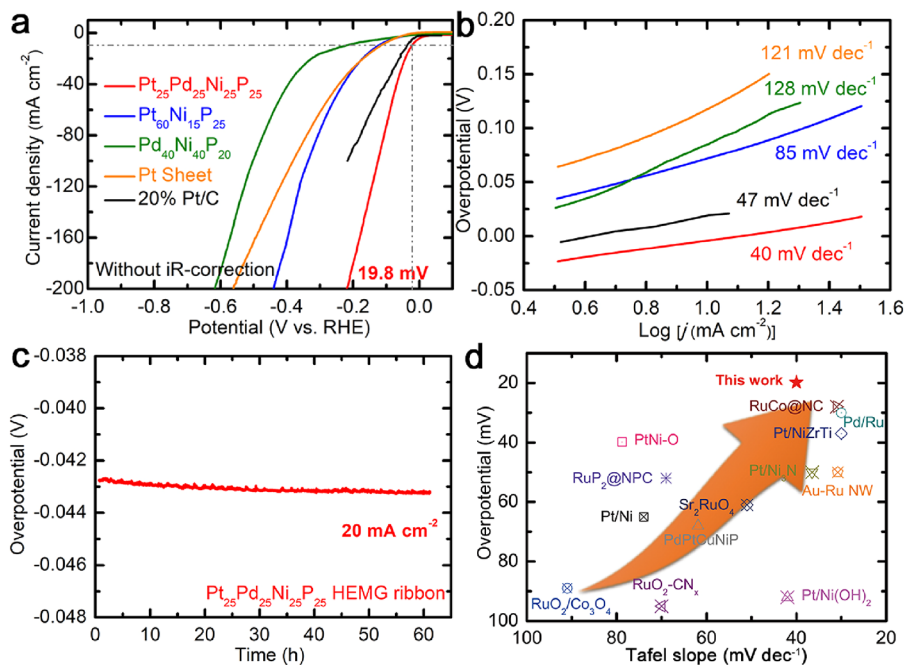


Figure 3. (a) HER polarization curves and (b) Tafel slopes of the MGs, (c) HER stability performance of the $\text{Pt}_{25}\text{Pd}_{25}\text{Ni}_{25}\text{P}_{25}$ HEMG, (d) comparison of the HER performance with recently reported noble-metal-based electrocatalysts in 1.0 M KOH solution.

subnanoscale, indicating the structure of the $\text{Pt}_{25}\text{Pd}_{25}\text{Ni}_{25}\text{P}_{25}$ HEMG possess local ordering in subnanoscale, which is in accordance with other reports.^{23,24} Note that the accurate quantification of Pt and P was not achievable in an energy-dispersive X-ray spectroscopy (EDS) spectrum because of their inevitable signal overlapping. Accordingly, we employed inductively coupled plasma–optical emission spectrometry (ICP-OES) and X-ray photoelectron spectrometry (XPS) to quantify the chemical compositions in the matrix and on the surface of the as-spun $\text{Pt}_{25}\text{Pd}_{25}\text{Ni}_{25}\text{P}_{25}$ HEMG, respectively (Figure 1f). The measured atomic ratios are very close to the theoretical equiatomic values. Figures S1 and S2 in the Supporting Information show the HRTEM and elemental mapping results of the $\text{Pt}_{60}\text{Ni}_{15}\text{P}_{25}$ and $\text{Pd}_{40}\text{Ni}_{40}\text{P}_{20}$ MGs, confirming their amorphous structures. The smooth surface morphology of the $\text{Pt}_{25}\text{Pd}_{25}\text{Ni}_{25}\text{P}_{25}$ HEMG was observed by scanning electron microscopy (SEM) and 3D atomic force microscopy (AFM) images (see Figures 1d and 1e). A nanoscale roughness (<14 nm) was detected in the AFM image, which would not be considered as having a significant effect on the following performance investigation since the HER performance was measured by the conversion of geometric surface area.

The amorphous structure of the as-spun $\text{Pt}_{25}\text{Pd}_{25}\text{Ni}_{25}\text{P}_{25}$ HEMG, as well as the $\text{Pt}_{60}\text{Ni}_{15}\text{P}_{25}$ and $\text{Pd}_{40}\text{Ni}_{40}\text{P}_{20}$ MGs, was further confirmed by XRD in Figure 2a. Broad diffuse diffraction peaks were obtained for the as-spun ribbons without any observations of crystalline peaks.²⁵ To elucidate the surface chemical valence states of the as-spun $\text{Pt}_{25}\text{Pd}_{25}\text{Ni}_{25}\text{P}_{25}$ HEMG, high-resolution XPS spectra of Pt 4f, Pd 3d, Ni 2p, P 2p, and O 1s were obtained, as shown in Figures 2b–f. The Pt 4f spectrum with the binding energy of 71.8 eV was assigned to the Pt^0 state (Figure 2b). The Pd 3d spectra exhibited two major peaks at 336.1 and 337.2 eV, corresponding to the Pd^0 and Pd^{2+} , respectively. The Ni 2p spectra consisted of three major peaks of 852.8, 856.1, and 858.1 eV, which were ascribed to the Ni^0 , Ni^{2+} , and Ni^{3+} states,

respectively. The P 2p spectra presented binding energies at 130.0, 131.0, and 132.6 eV, which can be assigned to P^{3-} , Ni–P, and PO_4^{3-} , respectively.^{19,26} The formation of PO_4^{3-} would promote rate-determining steps including water dissociation²⁷ and Gibbs free energies of hydrogen adsorption²⁸ during the HER process. The O 1s spectra exhibited three major peaks at the binding energies of 530.7, 531.8, and 533.2 eV, which could be ascribed to metal oxides, metal hydroxides, and adsorbed oxygen, respectively.²⁹ Such results demonstrated the formation of Ni oxides with a slight amount of Pd oxides on the surface. Meanwhile, the metal hydroxide was majorly attributed to the formation of $\text{NiOOH}/\text{Ni}(\text{OH})_3$.

The HER activity was performed by a standard three-electrode electrochemical station where the three as-spun ribbons were employed directly as a working electrode in 1.0 M KOH solution. The linear sweep voltammetry (LSV) curves of the ribbons were measured at a scan rate of 5 mV s^{-1} . It was found that the required overpotential at the current density of 10 mA cm^{-2} and the resulting Tafel slope of the $\text{Pt}_{25}\text{Pd}_{25}\text{Ni}_{25}\text{P}_{25}$ HEMG were 19.8 mV and 40 mV dec^{-1} , respectively, which was much improved compared to those of the $\text{Pt}_{60}\text{Ni}_{15}\text{P}_{25}$ and $\text{Pd}_{40}\text{Ni}_{40}\text{P}_{20}$ MGs, as well as the pure Pt sheet and Pt/C nanoparticles (Figures 3a and 3b), e.g., $\text{Pt}_{60}\text{Ni}_{15}\text{P}_{25}$ (105.1 mV and 85 mV dec^{-1}), $\text{Pd}_{40}\text{Ni}_{40}\text{P}_{20}$ (205.2 mV and 128 mV dec^{-1}), Pt sheet (103.2 mV and 121 mV dec^{-1}), and Pt/C (33.1 mV and 47 mV dec^{-1}). Such results demonstrate that a synergistic function of the Pt and Pd atoms plays an essential contribution to enhance the HER activity. More impressively, the achieved overpotential of the $\text{Pt}_{25}\text{Pd}_{25}\text{Ni}_{25}\text{P}_{25}$ HEMG was as low as 122.2 mV even at the current density of 100 mA cm^{-2} , further strengthening its potential industrial applications where a large current density is required.

With respect to the HER durability, chronoamperometry was conducted at the current density of 20 mA cm^{-2} for the $\text{Pt}_{25}\text{Pd}_{25}\text{Ni}_{25}\text{P}_{25}$ HEMG (Figure 3c). It was found that the overpotential could maintain essentially no change for 60 h,

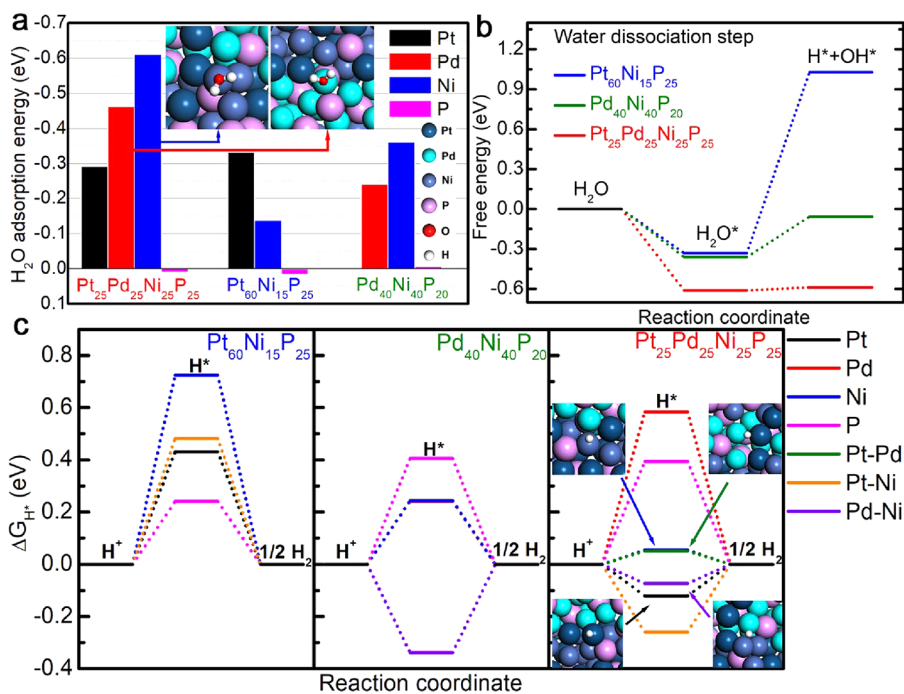


Figure 4. (a) DFT calculated adsorption energies of H₂O molecules on different exposed elemental sites of Pt₆₅Ni₁₅P₂₅, Pd₄₀Ni₄₀P₂₀, and Pt₂₅Pd₂₅Ni₂₅P₂₅. The insets in panel (a) show the local coordination environment of Ni and Pd sites in Pt₆₅Ni₁₅P₂₅. (b) Free-energy diagrams of reaction coordinate for water dissociation on the active sites of Pt₆₅Ni₁₅P₂₅, Pd₄₀Ni₄₀P₂₀, and Pt₂₅Pd₂₅Ni₂₅P₂₅. Both panels (a) and (b) demonstrated enhanced Volmer step of HER for Pt₂₅Pd₂₅Ni₂₅P₂₅. (c) Gibbs free-energy (ΔG_{H*}) profiles for various top and bridge sites of Pt₆₅Ni₁₅P₂₅, Pd₄₀Ni₄₀P₂₀ and Pt₂₅Pd₂₅Ni₂₅P₂₅. The insets show the local chemical environment of various H* adsorption sites with superior ΔG_{H*} in Pt₂₅Pd₂₅Ni₂₅P₂₅.

while ICP-OES results of the residual electrolyte show that the metal leaching concentrations of Pt, Pd, Ni, P were almost negligible (see Table S1 in the Supporting Information), suggesting a strong sustainable viability of the Pt₂₅Pd₂₅Ni₂₅P₂₅ HEMG. Moreover, to further emphasize the excellent structural stability, we also performed several characterizations on the evolutions of the structure, surface morphology, and surface chemical valent states for the previously used Pt₂₅Pd₂₅Ni₂₅P₂₅ HEMG (see Figures S3–S5 in the Supporting Information). The XRD result shows that the amorphous structure was well-retained for the previously used Pt₂₅Pd₂₅Ni₂₅P₂₅ HEMG (Figure S3). Nevertheless, it is notable that the surface states, including the morphology and chemical valences, presented an obvious evolution, that is, many spherical-like nanogranules precipitated on the surface (Figure S4) and the proportions of the chemical valences for Pt²⁺, Pd²⁺, Ni²⁺, and metal–oxygen were significantly improved (Figure S5). Such results demonstrate that new metal oxides were gradually formed, which is inevitable for such chemical reactivity.

To put the excellent HER performance of the Pt₂₅Pd₂₅Ni₂₅P₂₅ HEMG into perspective, we also summarized several state-of-the-art noble-metal-based electrocatalysts in Figure 3d, as well as Table S2 in the Supporting Information. It is noteworthy that the achieved HER activity of the Pt₂₅Pd₂₅Ni₂₅P₂₅ HEMG is better than that of our recently reported five-element melt-spun Pd₂₀Pt₂₀Cu₂₀Ni₂₀P₂₀ HEMG,¹⁹ which is attributed to the nonaddition of Cu atoms, which are considered as an inert element for the HER.³⁰ However, simply including a high amount of Pt or Pd is not the key factor to enhancing the HER activity in this work, because the Pt₂₅Pd₂₅Ni₂₅P₂₅ HEMG presents a 5-times-higher

performance than that of the Pt₆₀Ni₁₅P₂₅ MG (Figure 3a). This comparison clearly illustrates the synergistic effect of using a multicomponent HEMG. Finally, it is notable that the achieved HER activity of the Pt₂₅Pd₂₅Ni₂₅P₂₅ HEMG is better than that of reported electrocatalysts with ultrahigh specific surface areas such as honeycomb-like Pt/NiZrTi,²⁰ and even nanoparticles, nanowires, and two-dimensional catalysts,^{31–43} despite our melt-spun Pt₂₅Pd₂₅Ni₂₅P₂₅ HEMG possessing a smooth surface.

Figure S6 in the Supporting Information shows the electrochemical impedance spectroscopy (EIS) results of the three as-spun ribbons that was conducted in the frequency range between 0.1 to 100 Hz in 1.0 M KOH solution. The semicircle diameter of the Pt₂₅Pd₂₅Ni₂₅P₂₅ HEMG was much smaller than those of the Pt₆₀Ni₁₅P₂₅ and Pd₄₀Ni₄₀P₂₀ MGs, indicating a stronger charge transfer ability, which leads to a faster HER activity.^{44,45} Such results further emphasize the significant synergistic function of Pt and Pd functional atoms in contributing to the excellent electrocatalytic activity. Double-layer capacitances (*C*_{dl}), which typically correlate to the electrochemically active surface areas, were measured by cyclic voltammetry at various scan rates between 20 mV s⁻¹ and 100 mV s⁻¹ in the potential range of 0.1 to 0.2 V (RHE) for the three ribbons (see Figure S7 in the Supporting Information). The calculated *C*_{dl} value of the Pt₂₅Pd₂₅Ni₂₅P₂₅ HEMG was 5.71 mF cm⁻², which was significantly higher than those of the Pt₆₀Ni₁₅P₂₅ (3.83 mF cm⁻²) and Pd₄₀Ni₄₀P₂₀ (4.54 mF cm⁻²) MGs. Note that all three ribbons exhibited the same smooth surface morphology (see Figures 1d and 1e). The higher *C*_{dl} value suggested more electrochemically active sites for the Pt₂₅Pd₂₅Ni₂₅P₂₅ HEMG, compared to the Pt₆₀Ni₁₅P₂₅ and Pd₄₀Ni₄₀P₂₀ MGs, further evidencing the synergistic effect of

using both Pt and Pd in a high-entropy alloy for enhancement of the HER activity.

To elucidate the microscopic electrocatalytic mechanisms, local catalytic performance of various active sites was calculated using the density functional theory (DFT) method. According to the Tafel slope results in Figure 3b, the HER process of the Pt₂₅Pd₂₅Ni₂₅P₂₅ HEMG is the Volmer–Heyrovsky reaction, which involves two major steps: (1) adsorption and dissociation of H₂O molecules and (2) adsorption and desorption of H* for hydrogen evolution.⁴⁶ With respect to the Volmer step, the adsorption of H₂O molecules onto different elemental sites were investigated in Figure 4a. It reveals that the H₂O molecules prefer to adsorb on the top of each single metal atom; however, the P sites have almost no adsorption capacity of the H₂O molecules for the MG ribbons. Moreover, it was found that the synergistic function of Pt and Pd would greatly improve H₂O adsorption energy, especially at the Pd and Ni sites coordinated with Pt atoms (see insets in Figure 4a). To further clarify the physical origin of enhanced H₂O adsorption capacity of Pd and Ni sites in Pt₂₅Pd₂₅Ni₂₅P₂₅, local electron density difference after H₂O adsorption at the Pd and Ni sites of the ribbons were systematically analyzed (see Figures S8 and S9 in the Supporting Information). The results show that, although the equilibrium distance between Pd and O atom in Pt₂₅Pd₂₅Ni₂₅P₂₅ is farther than that in Pd₄₀Ni₄₀P₂₀ (2.38 Å vs. 2.316 Å), the capacity of electron loss and gain of Pd and O atom that occurred in Pt₂₅Pd₂₅Ni₂₅P₂₅ is stronger than that in Pd₄₀Ni₄₀P₂₀ (Figure S8), resulting in an improved H₂O adsorption capacity on the Pd sites in Pt₂₅Pd₂₅Ni₂₅P₂₅. Furthermore, it was also found that the electron gain ability of the O atom in H₂O at the Ni site in Pt₂₅Pd₂₅Ni₂₅P₂₅ is better than that in Pt₆₅Ni₁₅P₂₅ and Pd₄₀Ni₄₀P₂₀, respectively (see Figure S9). The equilibrium distance between the Ni and O atoms in Pt₂₅Pd₂₅Ni₂₅P₂₅ is closer than that in Pt₆₅Ni₁₅P₂₅ and Pd₄₀Ni₄₀P₂₀ (2.138 Å vs 2.461 and 2.192 Å), indicating that the electron transferability is enhanced which would promote the H₂O adsorption capacity. Partial density of states (PDOS) of the MG samples were also calculated to probe the interaction strength between atoms (Figures S10 and S11 in the Supporting Information).⁴⁷ It is noteworthy that the absorbed O atom from the H₂O molecules has a strong affinity at the Pd site of Pd₄₀Ni₄₀P₂₀ with significant hybridization energies centered at −9.9 and −6.4 eV, respectively (Figure S10), whereas a strong left shift of the interaction positions (−10.1 and −6.9 eV) from the Fermi level was observed in Pt₂₅Pd₂₅Ni₂₅P₂₅. Encouragingly, this strong left shift of the interaction positions away from the Fermi level were also observed for the Ni sites on Pt₂₅Pd₂₅Ni₂₅P₂₅ and for the O atom from the H₂O molecules (Figure S11). This left shift phenomenon indicates a relatively increased adsorption strength and would facilitate the H₂O adsorption capacity in the Pt₂₅Pd₂₅Ni₂₅P₂₅ HEMG. In addition, the performance of catalytic sites for the Volmer step is also typically evaluated by the energy barrier of H₂O dissociation (Figure 4b).⁴⁸ Note that, while the H₂O dissociation on the effective H₂O adsorption sites of Pt₆₅Ni₁₅P₂₅, Pd₄₀Ni₄₀P₂₀, and Pt₂₅Pd₂₅Ni₂₅P₂₅ are all thermodynamically upward, the required energy barrier for Pt₂₅Pd₂₅Ni₂₅P₂₅ is much lower than that for Pt₆₅Ni₁₅P₂₅ and Pd₄₀Ni₄₀P₂₀, indicating that the Pt₂₅Pd₂₅Ni₂₅P₂₅ exhibits the best H₂O dissociation capacity. Therefore, these simulation results imply that the efficient

Volmer step has a significant contribution to the superior HER performance of the Pt₂₅Pd₂₅Ni₂₅P₂₅ HEMG.

With respect to the H* adsorption and desorption processes (the Heyrovsky step), Gibbs free energies (ΔG_{H^*}) for various possible active sites in Pt₆₅Ni₁₅P₂₅, Pd₄₀Ni₄₀P₂₀, and Pt₂₅Pd₂₅Ni₂₅P₂₅ were systematically studied (Figure 4c), and the corresponding local atomic configurations around the catalytic sites are shown in Figures S12–S14 in the Supporting Information. It was found that all of the active sites in Pt₆₅Ni₁₅P₂₅ and Pd₄₀Ni₄₀P₂₀ show $|\Delta G_{H^*}|$ values of ≥ 0.24 eV, whereas a series of active sites in Pt₂₅Pd₂₅Ni₂₅P₂₅ present $|\Delta G_{H^*}|$ values of ≤ 0.12 eV. The insets in Figure 4c exhibit the beneficial synergistic functions of Pt and Pd in Pt₂₅Pd₂₅Ni₂₅P₂₅, such as the active bridge site of <Pt–Pd>, with both of them acting as coordination elements with active top sites of <Ni>, Pd coordinating with an active top site of <Pt>, and Pt coordinating with the active bridge site of <Pd–Ni>. Note that the local chemical environment of all these active sites simultaneously involves Pt and Pd, which has a significant contribution to the improved H* adsorption and desorption processes for the HER process in Pt₂₅Pd₂₅Ni₂₅P₂₅. To further unveil the excellent hydrogen evolution activity of the catalytic sites in Pt₂₅Pd₂₅Ni₂₅P₂₅, *d*-orbital partial density states (*d*-PDOS) of the high-performance active sites ($|\Delta G_{H^*}| \leq 0.12$ eV) were calculated in Figure S15 in the Supporting Information. The synergistic function of Pt and Pd in Pt₂₅Pd₂₅Ni₂₅P₂₅, which is regarded as either the addition of Pd in Pt₆₅Ni₁₅P₂₅ or the addition of Pt in Pd₄₀Ni₄₀P₂₀, would shift the *d*-band center of the active sites. For example, a right shift of the *d*-band center of the Pt site occurred with the addition of Pd in Pt₆₅Ni₁₅P₂₅ (Figure S15a), which enhanced the weak interaction between the H* and Pt sites (Figure 4c). Similarly, the addition of Pt in Pd₄₀Ni₄₀P₂₀ led to a left shift of the *d*-band center of the Pd site (Figure S15b), weakening the too strong interaction between the H* and Pd sites (Figure 4c). The right shift of the *d*-band center of Ni and left shift of the *d*-band center of the Pd–Ni site (Figures S15c and S15d) were also consistent with the corresponding variation of ΔG_{H^*} shown in Figure 4c. Additionally, the *d*-PDOS of the Pt–Pd site, which only exists in Pt₂₅Pd₂₅Ni₂₅P₂₅, was also calculated, as shown in Figure S16 in the Supporting Information. In particular, we analyzed the *d*-PDOS of Pt and Pd atoms in the Pt–Pd site and compared their *d*-band center with single Pt or Pd sites in Pt₂₅Pd₂₅Ni₂₅P₂₅. (The black dotted line in Figure S16 is exactly the red solid line in Figure S15a, while the red dotted line in Figure S16 is the red solid line in Figure S15b.) It was observed that the *d*-band center of the Pt site shifted left while the Pd site shifted right when Pt–Pd are coexisting in Pt₂₅Pd₂₅Ni₂₅P₂₅ (Figure S16). This tendency is beneficial for the shift of ΔG_{H^*} closer to zero. The Pt atom would assist single the Pd site to enhance the too weak interaction with H*, while the Pd atom would weaken the strong H* interaction on the single Pt site. Therefore, these results indicate that the synergistic function of Pt and Pd in our newly developed Pt₂₅Pd₂₅Ni₂₅P₂₅ HEMG has significant contribution to the Heyrovsky step of HER.

In summary, a high-entropy metallic glass (HEMG) with four equimolar components of Pt₂₅Pd₂₅Ni₂₅P₂₅ was prepared by a scalable metallurgical method. The Pt₂₅Pd₂₅Ni₂₅P₂₅ HEMG exhibited outstanding HER performance in 1.0 M KOH solution, and the ribbon form can be employed directly as a flexible, self-supported electrode. The achieved overpotential of the Pt₂₅Pd₂₅Ni₂₅P₂₅ HEMG at a current density of

10 mA cm⁻² was 19.8 mV, surpassing those of the Pt- and Pd-based MGs, as well as most state-of-the-art noble-metal-based electrocatalysts. The promoted HER performance was attributed to the synergistic function of the high-entropy alloy design, the long-range disordered amorphous structure, and the high density of unsaturated atomic configuration. This work provides a new insight into the development of bulk electrodes for water splitting applications. Future attention should be paid to the study of lower-cost HEMG electrodes with good glass-forming ability.

■ ASSOCIATED CONTENT

SI Supporting Information

The Supporting Information is available free of charge at <https://pubs.acs.org/doi/10.1021/acsmaterialslett.2c00371>.

Materials and methods; structural information on the as-spun Pt₆₀Ni₁₅P₂₅ and Pd₄₀Ni₄₀P₂₀ MGs (Figures S1 and S2); characterizations of the used Pt₂₅Pd₂₅Ni₂₅P₂₅ HEMG (Figures S3–S5); EIS measurement and cyclic voltammetry curves of the samples (Figures S6 and S7); additional DFT calculations (Figures S8–S16); ICP-OES results of the residual electrolyte after the stability test (Table S1); HER performance comparison (Table S2) (PDF)

■ AUTHOR INFORMATION

Corresponding Authors

Zhe Jia – School of Materials Science and Engineering, Jiangsu Key Laboratory for Advanced Metallic Materials, Southeast University, Nanjing 211189, China; School of Mechanical and Manufacturing Engineering, University of New South Wales (UNSW Sydney), Sydney NSW 2052, Australia; orcid.org/0000-0002-5063-8390; Email: zhejia@seu.edu.cn

Ligang Sun – School of Science, Harbin Institute of Technology, Shenzhen 518055, China; Email: sunligang@hit.edu.cn

Baolong Shen – School of Materials Science and Engineering, Jiangsu Key Laboratory for Advanced Metallic Materials, Southeast University, Nanjing 211189, China; orcid.org/0000-0002-0358-6540; Email: blshen@seu.edu.cn

Jamie J. Krzucic – School of Mechanical and Manufacturing Engineering, University of New South Wales (UNSW Sydney), Sydney NSW 2052, Australia; Email: j.krzucic@unsw.edu.au

Authors

Yiyuan Yang – School of Materials Science and Engineering, Jiangsu Key Laboratory for Advanced Metallic Materials, Southeast University, Nanjing 211189, China

Qing Wang – Laboratory for Microstructures Institute of Materials Science, Shanghai University, Shanghai 200072, China

Charlie Kong – Electron Microscope Unit, University of New South Wales (UNSW Sydney), Sydney, NSW 2052, Australia

Yin Yao – Electron Microscope Unit, University of New South Wales (UNSW Sydney), Sydney, NSW 2052, Australia

Qianqian Wang – School of Materials Science and Engineering, Jiangsu Key Laboratory for Advanced Metallic Materials, Southeast University, Nanjing 211189, China; School of Materials Science and Engineering, Jiangsu Key

Laboratory of Advanced Structural Materials and Application Technology, Nanjing Institute of Technology, Nanjing 211167, China

Complete contact information is available at:

<https://pubs.acs.org/doi/10.1021/acsmaterialslett.2c00371>

Notes

The authors declare no competing financial interest.

■ ACKNOWLEDGMENTS

The authors acknowledge the facilities and the scientific and technical assistance of Microscopy Australia at the Electron Microscope Unit (EMU) within the Mark Wainwright Analytical Centre (MWAC) at UNSW Sydney. The authors acknowledge use of facilities and the assistance of Dr. Dorothy Yu and Dr. Yu Wang in the Solid State & Elemental Analysis Unit at Mark Wainwright Analytical Centre at UNSW Sydney. The authors acknowledge the use of the facilities and the scientific and technical assistance of the Microscopy Australia node at the University of Sydney (Sydney Microscopy & Microanalysis). This work was supported by the Fundamental Research Funds for the Central Universities (Grant No. 2242022R10010); the National Natural Science Foundation of China (Grant No. 51631003); the Australian Research Council (Discovery Grant No. DP180101393); the National Natural Science Foundation of China (NSFC No, 51871140); Natural Science Foundation of Jiangsu Province (Grant No. BK20191269); the National Natural Science Foundation of China (Project No. 12002108); the Guangdong Basic and Applied Basic Research Foundation (Project Nos. 2020A1515110236, 2022A1515011402); the Shenzhen Municipal Science and Technology Innovation Council (Project Nos. GXWD20201230155427003-20200824105236001, ZDSYS20210616110000001).

■ REFERENCES

- (1) Wang, C.; Qi, L. Hollow Nanosheet Arrays Assembled by Ultrafine Ruthenium–Cobalt Phosphide Nanocrystals for Exceptional pH-Universal Hydrogen Evolution. *ACS Mater. Lett.* **2021**, *3*, 1695–1701.
- (2) Xie, Y.; Cai, J.; Wu, Y.; Hao, X.; Bian, Z.; Niu, S.; Yin, X.; Pei, Z.; Sun, D.; Zhu, Z.; Lu, Z.; Niu, D.; Wang, G. Atomic Disorder Enables Superior Catalytic Surface of Pt-Based Catalysts for Alkaline Hydrogen Evolution. *ACS Mater. Lett.* **2021**, *3*, 1738–1745.
- (3) Liu, X.; Zou, P.; Song, L.; Zang, B.; Yao, B.; Xu, W.; Li, F.; Schroers, J.; Huo, J.; Wang, J.-Q. Combinatorial High-Throughput Methods for Designing Hydrogen Evolution Reaction Catalysts. *ACS Catal.* **2022**, *12*, 3789–3796.
- (4) Ju, S.; Feng, J.; Zou, P.; Xu, W.; Wang, S.; Gao, W.; Qiu, H.-J.; Huo, J.; Wang, J.-Q. A robust self-stabilized electrode based on Al-based metallic glasses for a highly efficient hydrogen evolution reaction. *J. Mater. Chem. A* **2020**, *8*, 3246–3251.
- (5) Yang, X.; Xu, W.; Cao, S.; Zhu, S.; Liang, Y.; Cui, Z.; Yang, X.; Li, Z.; Wu, S.; Inoue, A.; Chen, L. An amorphous nanoporous PdCuNi-S hybrid electrocatalyst for highly efficient hydrogen production. *Appl. Catal. B: Environ.* **2019**, *246*, 156–165.
- (6) Yu, T.; Zhang, Y.; Hu, Y.; Hu, K.; Lin, X.; Xie, G.; Liu, X.; Reddy, K. M.; Ito, Y.; Qiu, H.-J. Twelve-Component Free-Standing Nanoporous High-Entropy Alloys for Multifunctional Electrocatalysis. *ACS Mater. Lett.* **2021**, 181–189.
- (7) Li, R.; Liu, X.; Liu, W.; Li, Z.; Chan, K. C.; Lu, Z. Design of Hierarchical Porosity Via Manipulating Chemical and Microstructural Complexities in High-Entropy Alloys for Efficient Water Electrolysis. *Adv. Sci.* **2022**, *9*, 2105808.

- (8) Gludovatz, B.; Hohenwarter, A.; Catoor, D.; Chang, E. H.; George, E. P.; Ritchie, R. O. A fracture-resistant high-entropy alloy for cryogenic applications. *Science* **2014**, *345*, 1153–1158.
- (9) Qiu, Y.; Thomas, S.; Gibson, M. A.; Fraser, H. L.; Birbilis, N. Corrosion of high entropy alloys. *NPJ. Mater. Degrad.* **2017**, *1*, 15.
- (10) Qiu, H.-J.; Fang, G.; Wen, Y.; Liu, P.; Xie, G.; Liu, X.; Sun, S. Nanoporous high-entropy alloys for highly stable and efficient catalysts. *J. Mater. Chem. A* **2019**, *7*, 6499–6506.
- (11) Zhang, G.; Ming, K.; Kang, J.; Huang, Q.; Zhang, Z.; Zheng, X.; Bi, X. High entropy alloy as a highly active and stable electrocatalyst for hydrogen evolution reaction. *Electrochim. Acta* **2018**, *279*, 19–23.
- (12) Jia, Z.; Yang, T.; Sun, L.; Zhao, Y.; Li, W.; Luan, J.; Lyu, F.; Zhang, L.-C.; Kruzic, J. J.; Kai, J.-J.; Huang, J. C.; Lu, J.; Liu, C. T. A Novel Multinary Intermetallic as an Active Electrocatalyst for Hydrogen Evolution. *Adv. Mater.* **2020**, *32*, 2000385.
- (13) Chen, Z.-J.; Zhang, T.; Gao, X.-Y.; Huang, Y.-J.; Qin, X.-H.; Wang, Y.-F.; Zhao, K.; Peng, X.; Zhang, C.; Liu, L.; Zeng, M.-H.; Yu, H.-B. Engineering Microdomains of Oxides in High-Entropy Alloy Electrodes toward Efficient Oxygen Evolution. *Adv. Mater.* **2021**, *33*, 2101845.
- (14) Zhang, L.-C.; Jia, Z.; Lyu, F.; Liang, S.-X.; Lu, J. A review of catalytic performance of metallic glasses in wastewater treatment: Recent progress and prospects. *Prog. Mater. Sci.* **2019**, *105*, 100576.
- (15) Glasscott, M. W.; Pendergast, A. D.; Goines, S.; Bishop, A. R.; Hoang, A. T.; Renault, C.; Dick, J. E. Electrosynthesis of high-entropy metallic glass nanoparticles for designer, multi-functional electrocatalysis. *Nat. Commun.* **2019**, *10*, 2650.
- (16) Liu, X.; Ju, S.; Zou, P.; Song, L.; Xu, W.; Huo, J.; Yi, J.; Wang, G.; Wang, J.-Q. Advanced catalyst for hydrogen evolution reaction by dealloying Al-based nanocrystalline alloys. *J. Alloys Compd.* **2021**, *880*, 160548.
- (17) Xu, W.; Zhu, S.; Liang, Y.; Cui, Z.; Yang, X.; Inoue, A. A nanoporous metal phosphide catalyst for bifunctional water splitting. *J. Mater. Chem. A* **2018**, *6*, 5574–5579.
- (18) Jia, Z.; Duan, X.; Zhang, W. C.; Wang, W. M.; Sun, H.; Wang, S.; Zhang, L. C. Ultra-sustainable Fe78Si9B13 metallic glass as a catalyst for activation of persulfate on methylene blue degradation under UV-Vis light. *Sci. Rep.* **2016**, *6*, 38520.
- (19) Jia, Z.; Nomoto, K.; Wang, Q.; Kong, C.; Sun, L.; Zhang, L.-C.; Liang, S.-X.; Lu, J.; Kruzic, J. J. A Self-Supported High-Entropy Metallic Glass with a Nanosponge Architecture for Efficient Hydrogen Evolution under Alkaline and Acidic Conditions. *Adv. Funct. Mater.* **2021**, *31*, 2101586.
- (20) Li, R.; Liu, X.; Wu, R.; Wang, J.; Li, Z.; Chan, K. C.; Wang, H.; Wu, Y.; Lu, Z. Flexible Honeycombed Nanoporous/Glassy Hybrid for Efficient Electrocatalytic Hydrogen Generation. *Adv. Mater.* **2019**, *31*, 1904989.
- (21) Wang, J. Q.; Liu, Y. H.; Chen, M. W.; Xie, G. Q.; Louzguine-Luzgin, D. V.; Inoue, A.; Perepezko, J. H. Rapid Degradation of Azo Dye by Fe-Based Metallic Glass Powder. *Adv. Funct. Mater.* **2012**, *22*, 2567–2570.
- (22) Jia, Z.; Zhao, Y.; Wang, Q.; Lyu, F.; Tian, X.; Liang, S.-X.; Zhang, L.-C.; Luan, J.; Wang, Q.; Sun, L.; Yang, T.; Shen, B. Nanoscale Heterogeneities of Non-Noble Iron-Based Metallic Glasses toward Efficient Water Oxidation at Industrial-Level Current Densities. *ACS Appl. Mater. Interfaces* **2022**, *14*, 10288–10297.
- (23) Liu, Y. H.; Wang, D.; Nakajima, K.; Zhang, W.; Hirata, A.; Nishi, T.; Inoue, A.; Chen, M. W. Characterization of Nanoscale Mechanical Heterogeneity in a Metallic Glass by Dynamic Force Microscopy. *Phys. Rev. Lett.* **2011**, *106*, 125504.
- (24) Zhu, F.; Song, S.; Reddy, K. M.; Hirata, A.; Chen, M. Spatial heterogeneity as the structure feature for structure–property relationship of metallic glasses. *Nat. Commun.* **2018**, *9*, 3965.
- (25) Jia, Z.; Duan, X.; Qin, P.; Zhang, W. C.; Wang, W. M.; Yang, C.; Sun, H.; Wang, S.; Zhang, L. C. Disordered Atomic Packing Structure of Metallic Glass: Toward Ultrafast Hydroxyl Radicals Production Rate and Strong Electron Transfer Ability in Catalytic Performance. *Adv. Funct. Mater.* **2017**, *27*, 1702258.
- (26) Qi, Z.; Lee, W. XPS study of CMP mechanisms of NiP coating for hard disk drive substrates. *Tribol. Int.* **2010**, *43*, 810–814.
- (27) Zhu, D.; Wang, L.; Qiao, M.; Liu, J. Phosphate ion functionalized CoP nanowire arrays for efficient alkaline hydrogen evolution. *Chem. Commun.* **2020**, *56*, 7159–7162.
- (28) Zhang, X.; Ji, J.; Yang, Q.; Zhao, L.; Yuan, Q.; Hao, Y.; Jin, P.; Feng, L. Phosphate Doped Ultrathin FeP Nanosheets as Efficient Electrocatalysts for the Hydrogen Evolution Reaction in Acid Media. *ChemCatChem.* **2019**, *11*, 2484–2489.
- (29) Zhang, N.; Feng, X.; Rao, D.; Deng, X.; Cai, L.; Qiu, B.; Long, R.; Xiong, Y.; Lu, Y.; Chai, Y. Lattice oxygen activation enabled by high-valence metal sites for enhanced water oxidation. *Nat. Commun.* **2020**, *11*, 4066.
- (30) Huang, H.; Jung, H.; Li, S.; Kim, S.; Han, J. W.; Lee, J. Activation of inert copper for significantly enhanced hydrogen evolution behaviors by trace ruthenium doping. *Nano Energy* **2022**, *92*, 106763.
- (31) Cao, Z.; Chen, Q.; Zhang, J.; Li, H.; Jiang, Y.; Shen, S.; Fu, G.; Lu, B.-a.; Xie, Z.; Zheng, L. Platinum-nickel alloy excavated nano-multipods with hexagonal close-packed structure and superior activity towards hydrogen evolution reaction. *Nat. Commun.* **2017**, *8*, 15131.
- (32) Liu, H.; Xia, G.; Zhang, R.; Jiang, P.; Chen, J.; Chen, Q. MOF-derived RuO₂/Co₃O₄ heterojunctions as highly efficient bifunctional electrocatalysts for HER and OER in alkaline solutions. *RSC Adv.* **2017**, *7*, 3686–3694.
- (33) Yu, X.; Zhao, J.; Zheng, L.-R.; Tong, Y.; Zhang, M.; Xu, G.; Li, C.; Ma, J.; Shi, G. Hydrogen Evolution Reaction in Alkaline Media: Alpha- or Beta-Nickel Hydroxide on the Surface of Platinum? *ACS Energy Lett.* **2018**, *3*, 237–244.
- (34) Wang, Y.; Chen, L.; Yu, X.; Wang, Y.; Zheng, G. Superb Alkaline Hydrogen Evolution and Simultaneous Electricity Generation by Pt-Decorated Ni₃N Nanosheets. *Adv. Energy Mater.* **2017**, *7*, 1601390.
- (35) Mahmood, J.; Li, F.; Jung, S.-M.; Okyay, M. S.; Ahmad, I.; Kim, S.-J.; Park, N.; Jeong, H. Y.; Baek, J.-B. An efficient and pH-universal ruthenium-based catalyst for the hydrogen evolution reaction. *Nat. Nanotechnol.* **2017**, *12*, 441.
- (36) Zhu, Y.; Tahini, H. A.; Hu, Z.; Dai, J.; Chen, Y.; Sun, H.; Zhou, W.; Liu, M.; Smith, S. C.; Wang, H.; Shao, Z. Unusual synergistic effect in layered Ruddlesden–Popper oxide enables ultrafast hydrogen evolution. *Nat. Commun.* **2019**, *10*, 149.
- (37) Bhowmik, T.; Kundu, M. K.; Barman, S. Growth of One-Dimensional RuO₂ Nanowires on g-Carbon Nitride: An Active and Stable Bifunctional Electrocatalyst for Hydrogen and Oxygen Evolution Reactions at All pH Values. *ACS Appl. Mater. Interfaces* **2016**, *8*, 28678–28688.
- (38) Su, J.; Yang, Y.; Xia, G.; Chen, J.; Jiang, P.; Chen, Q. Ruthenium-cobalt nanoalloys encapsulated in nitrogen-doped graphene as active electrocatalysts for producing hydrogen in alkaline media. *Nat. Commun.* **2017**, *8*, 14969.
- (39) Lu, Q.; Wang, A.-L.; Gong, Y.; Hao, W.; Cheng, H.; Chen, J.; Li, B.; Yang, N.; Niu, W.; Wang, J.; Yu, Y.; Zhang, X.; Chen, Y.; Fan, Z.; Wu, X.-J.; Chen, J.; Luo, J.; Li, S.; Gu, L.; Zhang, H. Crystal phase-based epitaxial growth of hybrid noble metal nanostructures on 4H/fcc Au nanowires. *Nat. Chem.* **2018**, *10*, 456–461.
- (40) Pu, Z.; Amiin, I. S.; Kou, Z.; Li, W.; Mu, S. RuP₂-Based Catalysts with Platinum-like Activity and Higher Durability for the Hydrogen Evolution Reaction at All pH Values. *Angew. Chem., Int. Ed.* **2017**, *56*, 11559–11564.
- (41) Zhao, Z.; Liu, H.; Gao, W.; Xue, W.; Liu, Z.; Huang, J.; Pan, X.; Huang, Y. Surface-Engineered PtNi-O Nanostructure with Record-High Performance for Electrocatalytic Hydrogen Evolution Reaction. *J. Am. Chem. Soc.* **2018**, *140*, 9046–9050.
- (42) Luo, Y.; Luo, X.; Wu, G.; Li, Z.; Wang, G.; Jiang, B.; Hu, Y.; Chao, T.; Ju, H.; Zhu, J.; Zhuang, Z.; Wu, Y.; Hong, X.; Li, Y. Mesoporous Pd@Ru Core–Shell Nanorods for Hydrogen Evolution Reaction in Alkaline Solution. *ACS Appl. Mater. Interfaces* **2018**, *10*, 34147–34152.

(43) Shao, G.; Wang, Q.; Miao, F.; Li, J.; Li, Y.; Shen, B. Improved catalytic efficiency and stability by surface activation in Fe-based amorphous alloys for hydrogen evolution reaction in acidic electrolyte. *Electrochim. Acta* **2021**, *390*, 138815.

(44) Jia, Z.; Wang, Q.; Sun, L.; Wang, Q.; Zhang, L.-C.; Wu, G.; Luan, J.-H.; Jiao, Z.-B.; Wang, A.; Liang, S.-X.; Gu, M.; Lu, J. Attractive In Situ Self-Reconstructed Hierarchical Gradient Structure of Metallic Glass for High Efficiency and Remarkable Stability in Catalytic Performance. *Adv. Funct. Mater.* **2019**, *29*, 1807857.

(45) Jia, Z.; Jiang, J.-L.; Sun, L.; Zhang, L.-C.; Wang, Q.; Liang, S.-X.; Qin, P.; Li, D.-F.; Lu, J.; Kruzic, J. J. Role of Boron in Enhancing Electron Delocalization to Improve Catalytic Activity of Fe-Based Metallic Glasses for Persulfate-Based Advanced Oxidation. *ACS Appl. Mater. Interfaces* **2020**, *12*, 44789–44797.

(46) Subbaraman, R.; Tripkovic, D.; Strmcnik, D.; Chang, K. C.; Uchimura, M.; Paulikas, A. P.; Stamenkovic, V.; Markovic, N. M. Enhancing Hydrogen Evolution Activity in Water Splitting by Tailoring Li⁺-Ni(OH)₂-Pt Interfaces. *Science* **2011**, *334*, 1256–1260.

(47) Chen, Z.; Xu, Y.; Ding, D.; Song, G.; Gan, X.; Li, H.; Wei, W.; Chen, J.; Li, Z.; Gong, Z.; et al. Thermal migration towards constructing W-W dual-sites for boosted alkaline hydrogen evolution reaction. *Nat. Commun.* **2022**, *13*, 763.

(48) Li, F.; Han, G. F.; Noh, H. J.; Lu, Y. L.; Xu, J.; Bu, Y. F.; Fu, Z. P.; Baek, J. B. Construction of Porous Mo₃P/Mo Nanobelts as Catalysts for Efficient Water Splitting. *Angew. Chem.-Int. Ed.* **2018**, *57*, 14139–14143.